



Unveiling the dual charge modulation of built-in electric field in metal-free photocatalysts for efficient photo-Fenton-like reaction

Fengting He^a, Yangming Lu^a, Guofei Jiang^a, Yang Zhang^a, Pei Dong^a, Xiaoming Liu^a, Yongqiang Wang^{a,*}, Chaocheng Zhao^a, Shuaijun Wang^{b,*}, Xiaoguang Duan^c, Jinqiang Zhang^{c,*}, Shaobin Wang^c

^a State Key Laboratory of Petroleum Pollution Control, China University of Petroleum (East China), 66 West Changjiang Road, Qingdao 266580, PR China

^b School of Energy and Power Engineering, Jiangsu University, Zhenjiang 212013, PR China

^c School of Chemical Engineering, The University of Adelaide, North Terrace, Adelaide, SA 5005, Australia

ARTICLE INFO

Keywords:

Carbon nitride
Built-in electric field
Dual mechanism
Charge modulation
Photo-Fenton-like reaction

ABSTRACT

Herein, we delved into the dual charge modulation of built-in electric field (BIEF) within photocatalysts on degradation of bisphenol A (BPA) via a photocatalysis coupling peroxymonosulfate activation (PC-PMS) system. Thiophene rings were incorporated into the carbon nitride conjugated structure (CN-TDC-X) to tailor the BIEF for enhanced PC-PMS mediated wastewater purification. Advanced characterizations and theoretical calculations confirmed that CN units of the planar heterojunction acted as electron donors in the dark, activating PMS to generate reactive oxygen species of $\text{SO}_4^{\bullet-}$ and $\bullet\text{OH}$, and facilitating electron transfer process (ETP) via non-radical pathways. While the motifs containing thiophene rings served as electron donors under light irradiation, initiating the production of h^+ , $\text{O}_2^{\bullet-}$, $^1\text{O}_2$, and activating the ETP pathway. The dual sites modulation by BIEF contributed to the efficient degradation of BPA in PC-PMS system. The work provides valuable insights into the manipulator in photo-Fenton-like process for sustainable and environmentally-friendly water purification.

1. Introduction

Water scarcity has become a pressing global issue, with an estimated 5 billion people projected to face severe water scarcity by 2050. Therefore, the development of effective technologies for wastewater treatment and recycling is of increasing importance [1–3]. Photocatalysis coupling of peroxymonosulfate activation (PC-PMS) has emerged as a powerful strategy for the removal of persistent organic contaminants from wastewater. PC-PMS utilizes photo-excited hot carriers in photochemical process and active sites on heterogeneous catalytic process to activate highly reactive species such as $\text{SO}_4^{\bullet-}$ (2.5 – 3.1 V vs normal hydrogen electrode (NHE)) and $\bullet\text{OH}$ (1.8 – 2.7 V vs NHE), effectively harnessing sunlight to eliminate micropollutants [4–6]. Although significant progress has been made in the use of metal-based photocatalysts for PC-PMS process, the resulting metal-containing sludge poses a risk of secondary pollution, limiting their practical applications [7,8]. Consequently, recent research has focused on the selection of metal-free semiconductor photocatalysts to advance PC-PMS technology.

Polymeric carbon nitride (CN) exhibits highly advantageous properties, including non-toxicity, stability, and superior optical properties, making it an excellent candidate for PC-PMS processes [9,10]. CN acts as a heterogeneous catalyst, with its active site enabling the activation of PMS into reactive oxygen species. Additionally, the photoexcited hot carriers (i.e., electron and hole) in CN serve as another driving force to facilitate PMS initiation. These two processes synergistically contribute to the effective removal of pollutants. However, the practical application of PC-PMS technology using CN has been limited by the low light harvesting efficiency, sluggish charge dynamics, and fatigue catalytic activity. For example, Zhang et al. [11] reported that a C_3N_4 -based PC-PMS system achieved only a 10% removal efficiency of BPA in 60 min, highlighting the suboptimal catalytic performance of pure g- C_3N_4 in PMS activation. Therefore, it is highly desirable to uncover the factors influencing heterogeneous catalysis and the photochemical process in PC-PMS, to develop robust catalysts that enable highly efficient wastewater purification.

Built-in electric field (BIEF) of heterogeneous catalysts plays a pivotal role in shaping catalytic reactions [12]. This field has been

* Corresponding authors.

E-mail addresses: wangyq@upc.edu.cn (Y. Wang), shuaijunwang@ujs.edu.cn (S. Wang), jinqiang.zhang@adelaide.edu.au (J. Zhang).

<https://doi.org/10.1016/j.apcatb.2023.123307>

Received 27 June 2023; Received in revised form 14 September 2023; Accepted 15 September 2023

Available online 16 September 2023

0926-3373/© 2023 The Authors. Published by Elsevier B.V. This is an open access article under the CC BY-NC-ND license (<http://creativecommons.org/licenses/by-nc-nd/4.0/>).

shown to modulate the electronic properties of catalysts, facilitating the adsorption and activation of reactant molecules and ultimately enhancing catalytic activity [13]. Moreover, in photocatalytic systems, the BIEF can enhance charge dynamics within the photocatalysts, enabling efficient utilization of the full spectrum of sunlight and promoting photochemical processes. Therefore, understanding the role of BIEF in the PC-PMS process is essential for designing and optimizing catalytic systems with improved performance, selectivity, and sustainability. However, this aspect of PC-PMS remains largely unexplored and warrants further investigation.

In this study, we adopted a copolymerization process to incorporate thiophene rings into the carbon nitride conjugated structure (CN-TDC-X), with the aim of tailoring the BIEF for enhanced PC-PMS mediated wastewater purification, including the degradation of bisphenol A (BPA) and real wastewater treatment, and unveiling the catalyst structure-performance relationships. Advanced characterizations and density functional theory (DFT) calculation results elucidated the influence of BIEF on the dual charge modulation mechanism within the PC-PMS system. CN unit in CN-TDC-40 functioned as the electron donor in the absence of light, facilitating the activation of PMS into $\text{SO}_4^{\bullet-}$, $\bullet\text{OH}$, and initiating electron transfer process (ETP) non-radical process. Upon visible light irradiation, the component of CN-TDC-40 served as an electron donor, effectively reducing PMS to generate the reactive oxygen species (ROS) of $\text{O}_2^{\bullet-}$ and $^1\text{O}_2$ and initiating ETP non-radical pathway. The BIEF-enabled directional migration of photoexcited hot carriers maximized the utilization of electron-hole pairs, resulting in significant improvements in both heterogeneous catalysis and photocatalytic activation of PMS. These findings provide a novel perspective on BIEF-mediated PC-PMS activation for the degradation of organic pollutants and offer valuable insights for the development of advanced and sustainable wastewater treatment technologies.

2. Experimental section

2.1. Chemicals

Urea ($\text{CO}(\text{NH}_2)_2$), potassium peroxymonosulfate ($\text{KHSO}_5 \cdot 0.5\text{KHSO}_4 \cdot 0.5 \text{K}_2\text{SO}_4$, PMS), 2,5-thiophenedicarboxaldehyde ($\text{C}_6\text{H}_4\text{O}_2\text{S}$, TDC), p-chlorobenzoic acid ($\text{C}_7\text{H}_5\text{ClO}_2$, p-CBA, 99%), bisphenol A ($\text{C}_{15}\text{H}_{16}\text{O}_2$, BPA, >99.0%), tetracycline hydrochloride ($\text{C}_{22}\text{H}_{25}\text{ClN}_2\text{O}_8$, TC, >99.0%), rhodamine B ($\text{C}_{28}\text{H}_{31}\text{ClN}_2\text{O}_3$, RhB, >99.0%), p-Hydroxybenzoic acid ($\text{C}_7\text{H}_6\text{O}_3$, p-HBA, 99%), tert-butyl alcohol ($\text{C}_4\text{H}_{10}\text{O}$, TBA, >99.0%), ethylenediaminetetraacetic acid disodium salt ($\text{C}_{10}\text{H}_{14}\text{N}_2\text{Na}_2\text{O}_8$, EDTA, >99.0), methanol (CH_3OH , MeOH, >99.0%), 2,2,6,6-tetramethyl-4-piperidine ($\text{C}_9\text{H}_{19}\text{N}$, TEMP, >99%), nitro tetrazoliumbue chloride ($\text{C}_{40}\text{H}_{30}\text{Cl}_2\text{N}_{10}\text{O}_6$, NBT, 99%), isopropyl alcohol ($\text{C}_3\text{H}_8\text{O}$, IPA, >99.9%), 5,5-dimethyl-1-pyrroline-N-oxide ($\text{C}_6\text{H}_{11}\text{NO}$, DMPO, 97%), singlet oxygen sensor green (SOSG) probe, sodium chloride (NaCl), potassium carbonate (K_2CO_3), sodium dihydrogen phosphate (NaH_2PO_4), sodium sulfate (Na_2SO_4), sodium bicarbonate (NaHCO_3), sodium nitrate (NaNO_3), and deuterium oxide (D_2O , >99%) were used without any contaminations.

2.2. Synthesis of CN and thiophene rings modified CN (CN-TDC-X)

A copolymerization method was adopted to synthesize CN-TDC-X (X = 20, 40, and 60). Initially, 20 g of urea was dissolved in 20 mL of ultrapure water to form a homogeneous solution. Then, a certain amount (20, 40, and 60 mg) of 2,5-thiophenedicarboxaldehyde (TDC) was added to the solution and stirred for 12 h, followed by heating at 80 °C to remove the water. The obtained solid was fully ground and transferred into a lidded alumina crucible, which was calcined in air at 550 °C for 2 h with a ramping rate of 5 °C min⁻¹. For comparison, CN was prepared by direct calcination of urea in the air at 550 °C for 2 h with a ramping rate of 5 °C min⁻¹.

2.3. Activity evaluation

PC-PMS degradation of BPA was performed in a 100 mL reactor under visible-light irradiation, maintaining the temperature at 25 °C. 20 mg of photocatalyst was added to 100 mL of BPA solution (10 mg L⁻¹), and the mixture was magnetically stirred for 60 min in the dark to achieve adsorption-desorption equilibrium. Subsequently, PMS (0.5 mM) was added to initiate the reaction under visible light irradiation. A 300 W Xeon lamp with a cutoff filter ($\lambda > 420 \text{ nm}$) was employed as the light source. At 10-min intervals, 1.5 mL of the solution was withdrawn and filtered with membrane filters (0.22 μm), which was then mixed with 0.5 mL of methanol to quench the radical species. The concentrations and intermediates of collected samples were analyzed using a liquid chromatography-mass spectrometry (HPLC-MS/MS) equipped with an SPD-20A UV/Vis detector at the detection wavelength of 276 nm. Further details regarding the HPLC settings are provided in Text S1. For comparisons, photocatalytic and heterogeneous catalytic BPA degradation were assessed in the absence of PMS and light irradiation, respectively. Moreover, the kinetics results with the photocatalysts may have been affected by the differences in optical thickness of the reactor at the concentration used with each catalyst specimens [14–17]. Therefore, it is necessary to evaluate the value of the optical thickness in the reactor with catalyst specimen. The detailed results are presented in Fig. S1.

2.4. Analytical methods

The removal efficiency of total organic carbon (TOC) was determined using a TOC-L CPH Shimadzu analyzer. EPR spectra was collected on a Bruker A300 EPR instrument with a Cool Edge cryo system (Bruker, German A). Spin trapping agent of 5, 5-dimethyl-1-pyrroline N-oxide (DMPO) was utilized to capture $\bullet\text{OH}$, $\text{SO}_4^{\bullet-}$, and $\text{O}_2^{\bullet-}$, and a probe such as 2,2,6,6-tetramethyl-4-piperidine (TEMP) was used to detect $^1\text{O}_2$. $^1\text{O}_2$ was also monitored by a singlet oxygen sensor green (SOSG) probe [18]. For the SOSG measurement, 100 μg of SOSG was dispersed in 330 μL of deoxygenated methanol to obtain a stock solution of SOSG (500 μM). Subsequently, 5 mg of CN-TDC-40 was dispersed into 100 mL of BPA solution, then 30 μL of SOSG solution and 15.4 mg PMS were added. The resulting solution was irradiated for 5 min. The obtained sample was filtered through a 0.22 μm filter and measured using a spectrofluorometer ($\lambda_{\text{ex}} = 488 \text{ nm}$ and $\lambda_{\text{em}} = 525 \text{ nm}$). The electrochemical tests are summarized in Text S2.

3. Results and discussion

3.1. Catalyst preparation and characterization

The synthesis of probing catalysts was illustrated in Fig. 1a and Fig. S2, wherein a Schiff base reaction was employed to incorporate thiophene aromatic rings into the conjugated system of CN. The process involved nucleophilic addition and dehydration reactions between the terminal amino group of the generated intermediates of melem/melamine (resulting from the polymerization of urea) and the aldehyde group on 2,5-thiophenedicarboxaldehyde (TDC). This series of reactions led to the formation of thiophene rings-functionalized CN (CN-TDC-X).

The morphologies of CN and CN-TDC-40 were examined using scanning electron microscope (SEM) and transmission electron microscopy (TEM) images (Fig. 1b-c and Fig. S3). CN exhibited folded nano-sheets (Fig. 1b and S3a), while the fusion of thiophene rings into the carbon nitride matrix resulted in a honeycomb structure composed of small flakes. Notably, CN-TDC-40 displayed thinner layers and more voids compared to the multilayer structure of CN (Fig. 1c and S3b). Furthermore, CN-TDC-40 exhibited lattice fringes with a slightly wider lattice spacing of 0.34 nm than that of CN (Fig. 1d). This change is attributed to the introduction of larger radius S atoms into the carbon nitride framework [19]. In addition, STEM mappings revealed an even

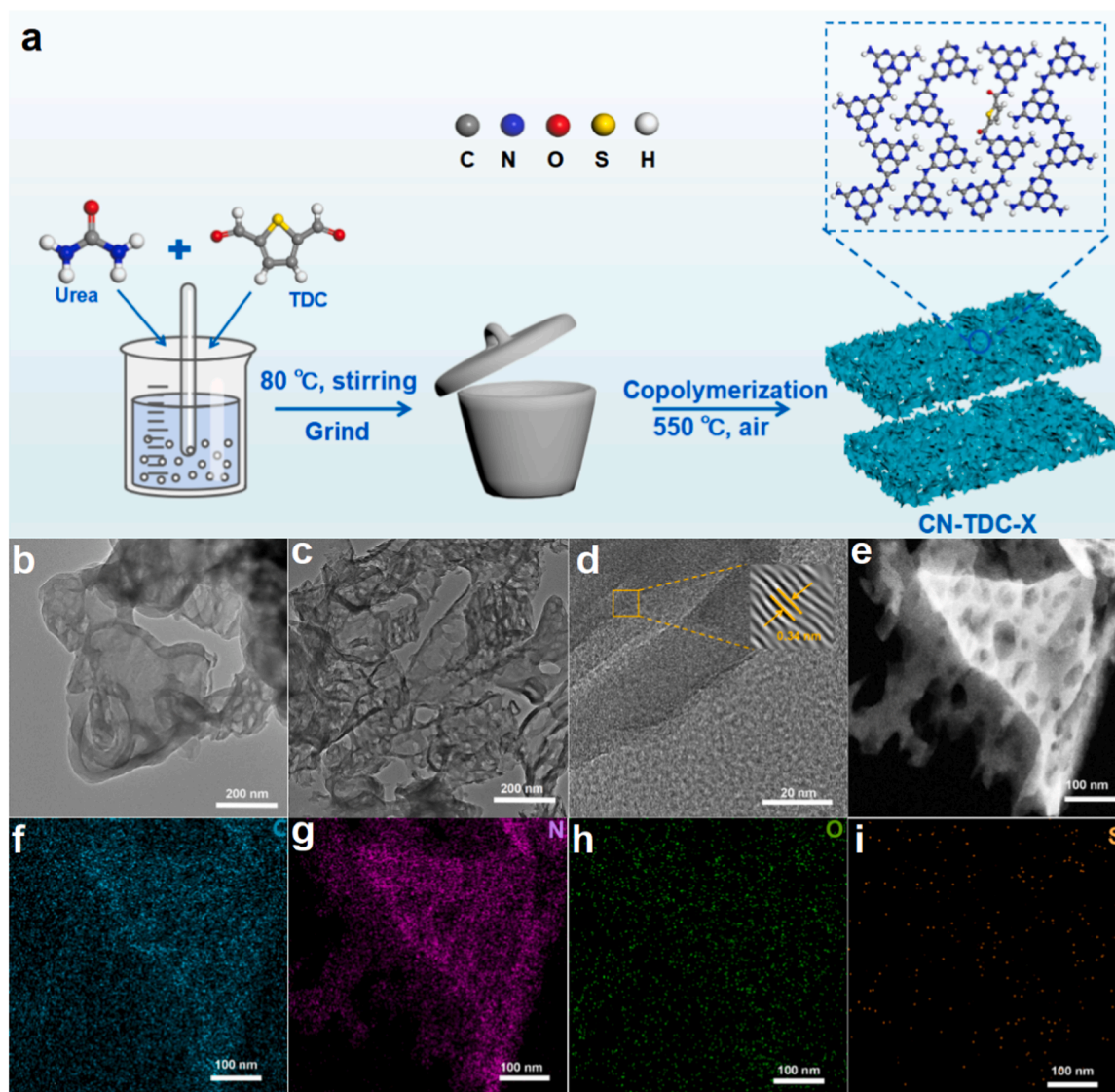


Fig. 1. Catalyst preparation and characterizations. (a) Schematic illustration of the synthetic process of CN-TDC-X; TEM images of (b) CN and (c) CN-TDC-40; (d) HRTEM image of CN-TDC-40; (e) HAADF-STEM image and (f-i) EDX mapping images of CN-TDC-40.

distribution of C, N, O, and S in CN-TDC-40 (Fig. 1e-i).

The crystal structures of CN and CN-TDC-X were analyzed through X-ray diffraction (XRD) patterns (Fig. 2a). CN displayed two prominent diffraction peaks at $2\theta = 13.1^\circ$ and 27.1° , corresponding to the (100) in-plane periodic triazine units and the (002) interlayer stacking, respectively [20]. The (002) peak shifted from 27.1° to 27.7° with the addition of TDC into the copolymerization process (Fig. 2b), indicating a decrease in the interlayer spacing and an increase in the interlaminar interaction on CN-TDC-X [21]. The molecular texture and functional groups of the as-prepared materials were investigated using Fourier transform infrared (FT-IR) spectroscopy. As shown in Fig. 2c, all the vibration bands in CN were observed in CN-TDC-X samples, indicating that the carbon nitride framework remained intact after the copolymerization of urea with TDC. The strong peaks observed at 809, 1200–1650, and 3000–3600 cm^{-1} were attributed to the stretching of C_3N_3 heterocycles, C_6N_7 units, and $-\text{NH}_2/\text{NH}/\text{OH}$ groups, respectively. In addition, a distinct absorption band at 620 and 420 cm^{-1} , attributed to the C–S stretching vibrations and the torsion of carbon ring [22,23], was observed in CN-TDC-X samples but was absent in CN. Notably, a new vibration representing the secondary amide (RCONHR') appeared at 1685 cm^{-1} (Fig. 2d), which clearly indicates the condensation of the

$-\text{COOH}$ group of TDC with the amino group of CN, marking the formation of terminal amide bond [24]. This observation suggests that the thiophene ring has been successfully incorporated into the carbon nitride matrix.

Solid-state ^{13}C NMR spectrum was used to verify the inclusion of thiophene rings into the CN network. As displayed in Fig. 2e, signal peaks centered at 156.1 and 164.6 ppm assigning to $\text{C}-\text{N}_3$ and CN_2-NH_2 , respectively, appeared in CN and CN-TDC-40 [25]. The result is consistent with XRD and FT-IR analysis, confirming the existence of heptazine structure in CN and CN-TDC-40. Noteworthy, a new peak assigned to the incorporated aromatic carbon was found at approximately 125 ppm [26], indicating the inclusion of aromatic carbon rings in the CN-TDC-40.

X-ray photoelectron spectroscopy (XPS) was carried out to scrutinize the chemical states in the catalysts. The full-scan spectra revealed the presence of C, N, and O elements (Fig. S4). The S content was too low to be detected, which was confirmed by the subsequent XPS S2p fine spectrum. In the high-resolution C 1s spectrum of CN, two peaks were observed at 284.8 and 288.1 eV, corresponding to extraneous carbon contaminant $\text{C}=\text{C}$ (sp^2) and the sp^2 $\text{N}-\text{C}=\text{N}$ bonding, respectively (Fig. 2f) [27]. On the other hand, the CN-TDC-40 sample displayed a

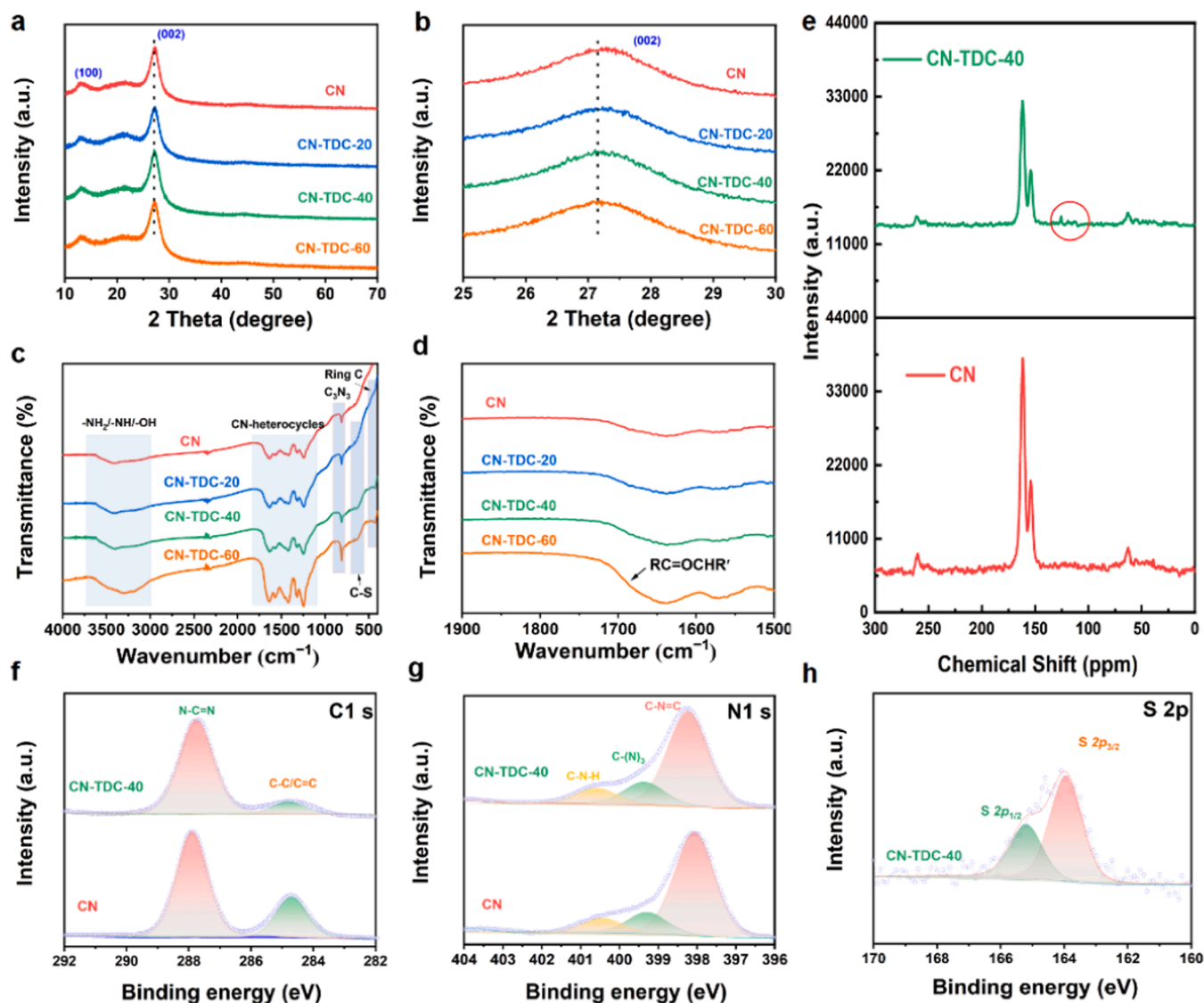


Fig. 2. Catalyst characterizations. (a) XRD patterns, (b) enlarged XRD patterns, (c) FT-IR spectra, (d) enlarged FT-IR patterns, (e) solid-state ^{13}C NMR spectrum, and XPS spectra of (f) C 1s, (g) N 1s, and (h) S 2p of CN and CN-TDC-X.

binding energy of the $\text{N}=\text{C}=\text{N}$ bond at 287.9 eV. The downshifted binding energy after the fusion of TDC into carbon nitride matrix indicated the interfacial interaction between TDC and CN unit for electron transferring. In N 1s spectra, three dominant peaks appeared at 398.5, 399.8, and 400.9 eV, which originated from $\text{C}-\text{N}=\text{C}$, $\text{N}-\text{C}_3$, and $\text{C}-\text{N}-\text{H}$ in CN, respectively (Fig. 2g). Furthermore, S 2p XPS spectra provides compelling evidence for the existence of thiophene groups within CN-TDC-40. This is evident from the presence of two distinctive signal peaks corresponding to C-S-C bonds inherent to the thiophene ring, as evidenced by the peaks at 163.8 eV ($\text{S } 2\text{p}_{3/2}$) and 165.2 eV ($\text{S } 2\text{p}_{1/2}$) (Fig. 2h). Notably, these peaks deviate from those observed in the conventional sulfur-doped CN, which typically exhibit peaks at 163.9 and 168.5 eV [28].

Elemental analysis (EA) of both CN and CN-TDC-X was performed to determine their C/N atomic ratio (Table S1). The C/N ratio of CN-TDC-X was found to be higher than that of CN. With an increase in the TDC dosage during the copolymerization process, the C/N ratio of CN-TDC-X gradually increased from 0.56 to 0.58, indicating the successful insertion of thiophene into the carbon nitride units. Moreover, an increase in S content was observed, from 0.17% in CN-TDC-20 to 0.46% in CN-TDC-60. Thus, the combined results of FTIR NMR, XPS, and EA suggest the

successful incorporation of thiophene groups into the CN structure.

N_2 adsorption-desorption isotherms were utilized to examine the textural properties of CN and CN-TDC-X samples (Fig. S5). The observed type-IV curves, along with the H3 hysteresis loop, indicated the presence of mesoporous structures in all photocatalysts [33]. Notably, the BET surface area of CN-TDC-20, CN-TDC-40, and CN-TDC-60 was found to be 53.6, 61.7, and 57.5 $\text{m}^2 \text{g}^{-1}$, respectively (Table S2), slightly higher than that of CN (47.6 $\text{m}^2 \text{g}^{-1}$). The inset of Fig. S5 illustrates the pore size distribution of the samples in micropores and mesopores. These results suggest that the incorporation of thiophene rings has a negligible impact on the specific surface area and pore structure of CN.

3.2. Evaluation of PC-PMS catalytic performance

BPA was selected as the target contaminant to assess the performance of CN and CN-TDC-X in PC-PMS driven degradation processes. In the heterogeneous PMS activation process without light (catalyst/PMS), the adsorption rate of CN and CN-TDC-X for BPA was poor, and the highest adsorption rate was only 3% after 1 h of adsorption. CN/PMS showed negligible degradation of BPA. Whereas, the degradation rate experienced an initial increase and then a decrease as more dosage of

TDC was added in the preparation of CN-TDC-X. Among the samples, CN-TDC-40/PMS demonstrated the highest degradation efficiency, reaching 25% (Fig. 3a). This finding confirmed that the molecular doping of TDC in CN effectively influences PMS activation and BPA removal. In the photocatalytic system, CN-TDC-X exhibited a higher BPA degradation rate compared to CN, with the degradation efficiency reaching 70% using CN-TDC-40 in 60 min (Fig. 3b). However, a notable trend emerged with further increases in TDC dosage in CN-TDC-60, wherein a pronounced inhibitory effect was observed for BPA degradation within both heterogeneous and photocatalytic systems. This outcome can be attributed to the excessive incorporation of thiophene rings, causing structural distortion of CN and thereby altering its electronic configuration and semiconducting attributes [29].

Importantly, the efficiency of BPA removal was significantly enhanced in a PC-PMS system with CN-TDC-40 (Vis/CN-TDC-40/PMS) (Fig. 3c), resulting in 100% degradation of BPA within 40 min. This is much higher than the Vis/CN/PMS system (~10%), indicating that CN-TDC-40 can effectively activate PMS to produce highly oxidative species. Furthermore, the kinetic analysis of BPA degradation revealed distinct differences between the samples. While Vis/CN/PMS followed a first-order kinetic with a rate constant of 0.0035 min^{-1} (Fig. 3d), Vis/

CN-TDC-40/PMS exhibited a two-stage reaction kinetics with rate constants of $k_1 = 0.0467 \text{ min}^{-1}$ and $k_2 = 0.1540 \text{ min}^{-1}$. These results highlight the excellent performance and unique degradation behavior of CN-TDC-X in the PC-PMS oxidation process. This behavior can be elucidated by attributing the initial stage to photocatalyst activation and the photoinduced species' contribution to BPA oxidation. The observed higher value of k_2 in comparison to k_1 implies an elevated generation of ROS during the second stage. This, in turn, initiates free radical chain reactions, driving the rapid and thorough oxidation of BPA [30].

Controlled experiments were also performed (Fig. 3e), where the PMS/Vis (~5%), CN-TDC-40/PMS (~25%), and Vis/CN-TDC-40 (~75%) systems within 60 min showed considerably lower degradation efficiencies compared to the Vis/CN-TDC-40/PMS (~100%) system within 40 min, highlighting the synergistic effect between photocatalysis and PMS activation in the catalytic oxidation of BPA. The corresponding kinetic features of BPA degradation in other Vis/CN-TDC-X/PMS systems were presented in Fig. S6. The potential practical applications of the catalysts were evaluated based on their reusability and stability. The Vis/CN-TDC-40/PMS system demonstrated consistently high effectiveness in degrading BPA, maintaining a removal rate of approximately 99% even after four consecutive cycles of testing

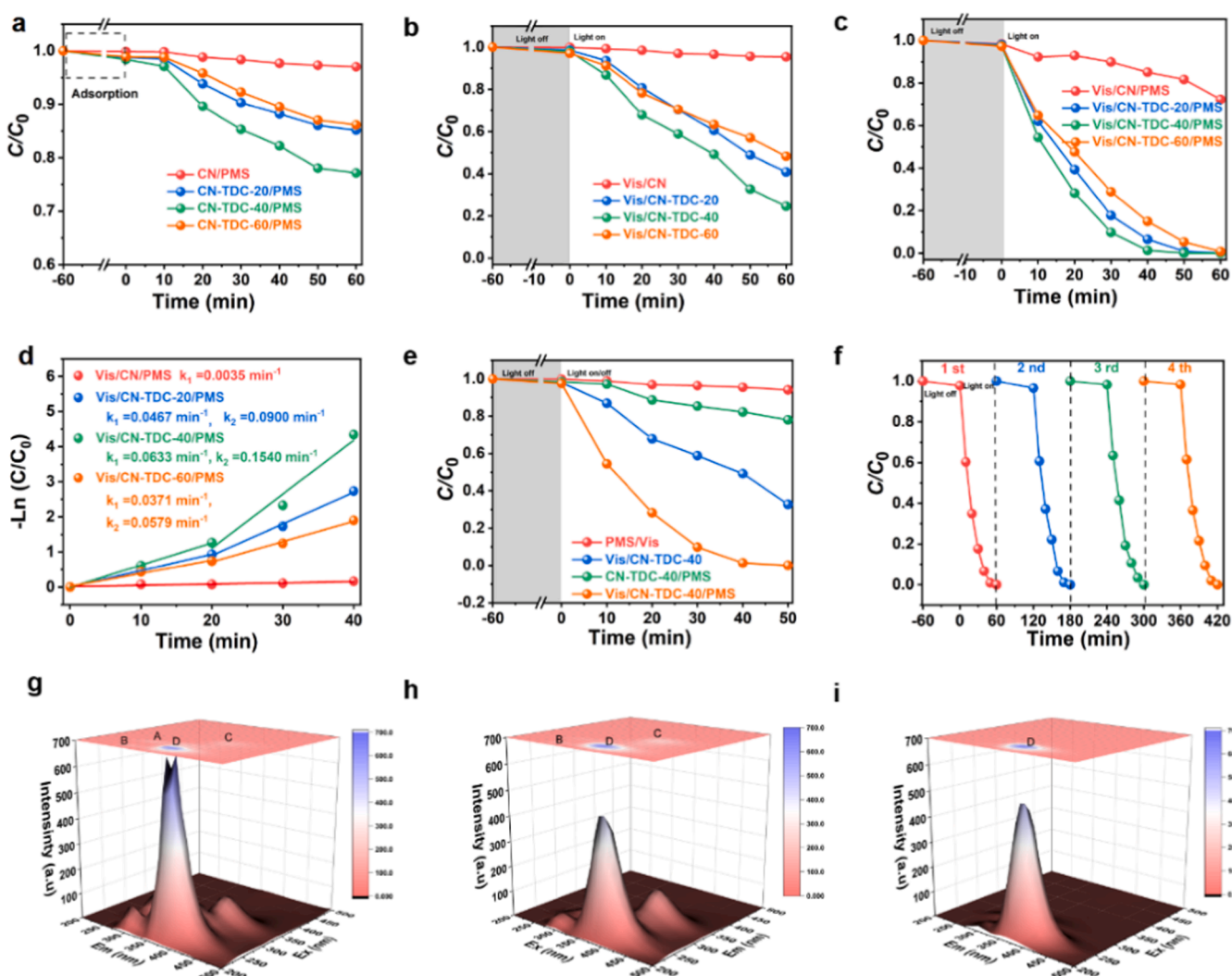


Fig. 3. BPA degradation efficiency using CN and CN-TDC-X under (a) heterogeneous PMS activation process in the dark, (b) photocatalytic system, and (c) PC-PMS system; (d) Kinetic plots for BPA degradation in Vis/CN/PMS and Vis/CN-TDC-40/PMS systems; (e) BPA degradation rate using CN-TDC-40 in different systems; (f) Stability test of CN-TDC-40 in PC-PMS driven BPA degradation for four cycles; 3D EEM fluorescence spectroscopy of grille outlet recorded at (g) 0 min, (h) 30 min, and (i) 60 min in Vis/CN-TDC-40/PMS. (Reaction conditions: [BPA] = 10 mg/L; [Catalyst] = 0.25 g L⁻¹; $\lambda > 420 \text{ nm}$, [PMS] = 0.5 mM, ambient temperature and without pH adjustment).

(Fig. 3f). Additionally, CN-TDC-40 exhibited strong resistance to interference from inorganic anions and displayed a wide pH adaptability range, as well as widely adaptability to the degradation of other pollutants (Fig. S7). The Vis/CN-TDC-40/PMS system was also tested using grid effluent from a sewage treatment plant (Table S3). The system achieved an efficiency of 71.7% for BPA degradation within 60 min and a mineralization rate of 60% for actual wastewater (Fig. S8a-b). The degradation performance of the Vis/CN-TDC-40/PMS system on actual wastewater was further analyzed using three-dimensional excitation-emission matrix spectroscopy (Fig. 3g-i). The fluorescence intensities of regions A (tyrosine aromatic proteins, $E_x/E_m=200\text{--}240/280\text{--}320$ nm), B (microbial metabolites, $E_x/E_m=260\text{--}280/280\text{--}320$ nm), C (humic acids, $E_x/E_m=300\text{--}360/380\text{--}440$ nm), and D (fulvic acids, $E_x/E_m=210\text{--}250/360\text{--}440$ nm) as well as BOD₅ aromatic proteins ($E_x/E_m=210\text{--}250/340\text{--}360$ nm), which correspond to different substances in urban wastewater, significantly decreased after 60 min of reaction, indicating the effective removal efficiency of the Vis/CN-TDC-40/PMS system for fluorescent substances. The fluorescence intensity of region D exhibited a trend of initially decreasing and then increasing, possibly due to the gradual degradation of component C into aromatic small molecule intermediates.

3.3. Identification of ROS

The degradation mechanism of the CN-TDC-40/PMS and Vis/CN-TDC-40/PMS systems was thoroughly investigated by monitoring reactive oxygen species (ROS) using various scavengers. Isopropyl alcohol (IPA) was used to quench $\cdot\text{OH}$, while methanol (MeOH) was employed as a scavenger for both $\text{SO}_4^{\cdot-}$ and $\cdot\text{OH}$ radicals in the PMS activation process [31,32]. ethylenediaminetetraacetic acid disodium salt (EDTA) was used to scavenge holes (h^+) [33]. In the photocatalytic system, p-benzoquinone (p-BQ) and furfuryl alcohol (FFA) were commonly used to capture superoxide radicals ($\text{O}_2^{\cdot-}$) and singlet oxygen ($^1\text{O}_2$), respectively. However, previous studies have suggested that p-BQ may overestimate the effect of $\text{O}_2^{\cdot-}$ by activating PMS to generate $^1\text{O}_2$, and FFA can react with PMS, hindering the release of other ROS [34]. Therefore, nitro tetrazolium chloride (NBT) and 2,2,6,6-tetramethyl-4-piperidone (TEMP) were used to quench the generation of $\text{O}_2^{\cdot-}$ and $^1\text{O}_2$, respectively. Moreover, singlet oxygen sensor green (SOSG), a highly selective $^1\text{O}_2$ fluorescent probe, was employed to identify the existence of $^1\text{O}_2$ [18].

In the heterogeneous PMS activation process, the CN-TDC-40/PMS system demonstrated the presence of active sites for PMS activation

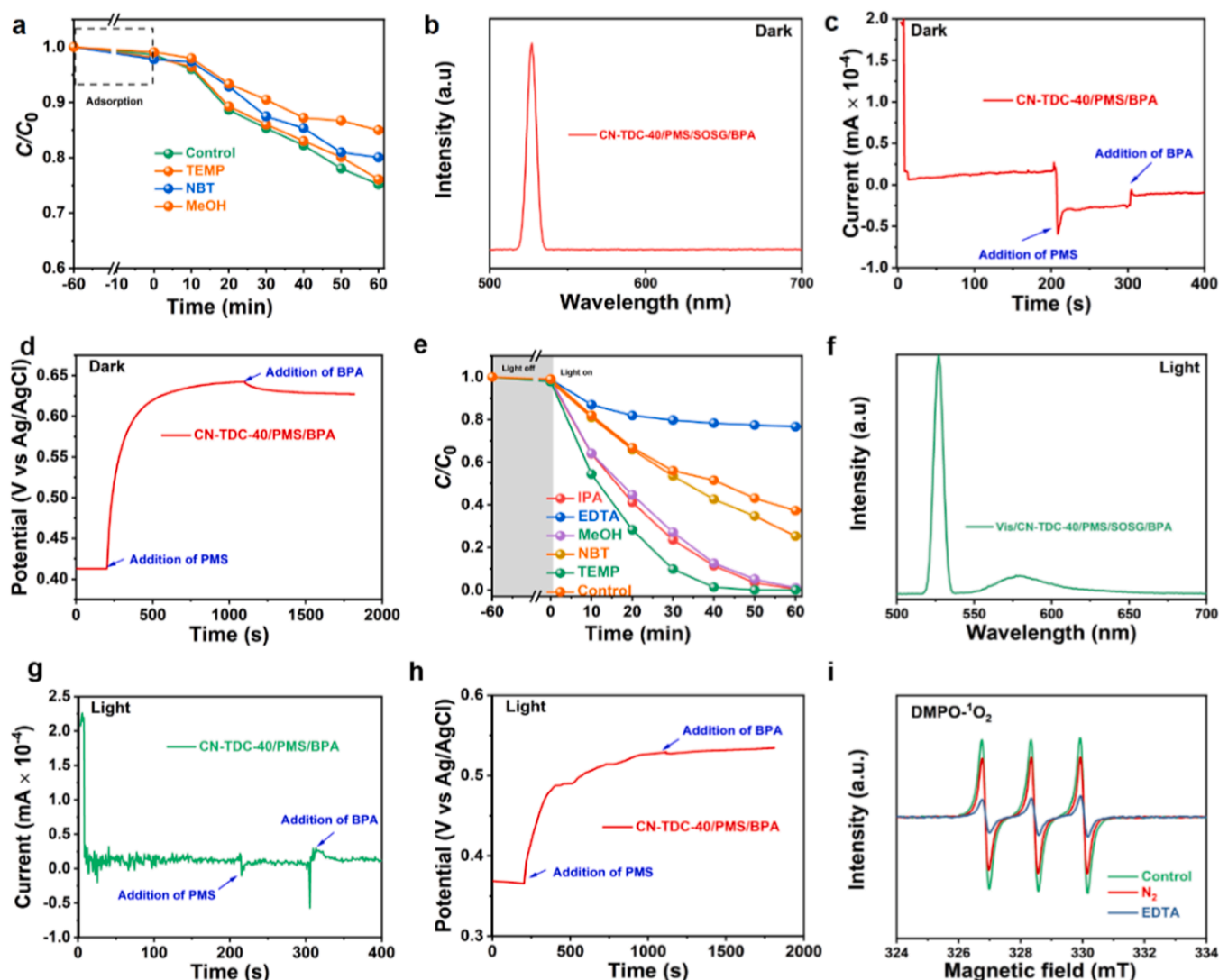


Fig. 4. (a) Quenching experiments, (b) fluorescence spectra of SOSG probing test, (c) CP measurements, and (d) OCP tests in the dark; (e) Quenching experiments, (f) fluorescence spectra of SOSG probing test, (g) CP measurements, (h) OCP tests under visible light irradiation; (i) EPR spectra for $^1\text{O}_2$ detection in Vis/CN-TDC-40/PMS system under N_2 atmosphere or in the presence of EDTA. (Conditions: [BPA] = 10 mg/L, [Catalyst] = 0.25 g L⁻¹, $\lambda > 420$ nm, [EDTA] = 20 mg, [PMS] = 0.5 mM, ambient temperature and without pH adjustment, no buffer).

on CN-TDC-40 by removing approximately 25% of BPA even in the absence of light illumination (Fig. 4a). The addition of MeOH and NBT inhibited the degradation of BPA, with MeOH having a greater inhibitory effect. A slight decline appeared after the addition of TEMP, indicating that $^1\text{O}_2$ played a negligible role in BPA degradation. Fig. 4b shows that no weak fluorescence signal was observed when SOSG was added (PMS/SOSG/BPA), further suggesting the absence of $^1\text{O}_2$ in the CN-TDC-40/PMS system. These findings indicate that $\text{SO}_4^{\bullet-}$ and $\bullet\text{OH}$ are the major ROS in the CN-TDC-40/PMS system.

The generation pathway of $\text{SO}_4^{\bullet-}$ and $\bullet\text{OH}$ was studied using chronoamperometric (CP) and open-circuit potential (OCP) measurements in the dark. In the CP test, immediate negative current was observed when PMS was injected into the CN-TDC-40 system, indicating direct electron transfer from CN-TDC-40 to PMS (Fig. 4c). A positive current was observed after adding BPA, revealing the electron transfer process (ETP) from absorbed BPA to the PMS-CN-TDC-40 complex. OCP measurement further reflected the kinetics of the charge-transfer process (Fig. 4d). The potential of CN-TDC-40 increased instantly upon the addition of PMS, indicating rapid electron transfer from CN-TDC-40 to PMS. Subsequently, the potential gradually declined with the addition of BPA, indicating the oxidation of BPA by PMS-CN-TDC-40 complex via ETP. These results confirm that PMS can be reduced to produce $\text{SO}_4^{\bullet-}$ and $\bullet\text{OH}$, as well as direct ETP processes, which are the main pathways for heterogeneous catalytic degradation of BPA.

The role of ROS in the PC-PMS system using CN-TDC-40 was also identified (Fig. 4e). The addition of IPA slightly decreased the BPA degradation efficiency to 88.6%, indicating a minor role of $\bullet\text{OH}$ in BPA degradation. MeOH had no apparent effect on the BPA removal rate (89.6%), suggesting that the contribution of $\text{SO}_4^{\bullet-}$ to BPA oxidation could be ignored. Whereas, the addition of EDTA led to a significant decrease in BPA removal (23.3%) in the Vis/CN-TDC-40/PMS system, indicating the dominating role of h^+ in BPA removal. Additionally, NBT and TEMP exhibited obvious inhibitory effects on BPA degradation, achieving only 48.4% and 57.4% in BPA removal within 40 min, respectively. This suggests that $\text{O}_2^{\bullet-}$ and $^1\text{O}_2$ also played significant roles in BPA degradation. Experiments using SOSG and solvent exchange further confirmed the presence of $^1\text{O}_2$. The CN-TDC-40/PMS/SOSG/BPA in the PC-PMS system showed a higher fluorescent intensity, implying the formation of $^1\text{O}_2$ (Fig. 4f). Furthermore, D_2O was used as a solvent to confirm the role of $^1\text{O}_2$, as its lifetime in D_2O is much higher than in H_2O , slightly accelerating BPA oxidation (Fig. S9). The reaction kinetics of Vis/CN-TDC-40/PMS in BPA degradation followed pseudo-first-order kinetics when the $\text{O}_2^{\bullet-}$, $^1\text{O}_2$, and h^+ were quenched (Fig. S10), while the second-stage kinetics remained after $\bullet\text{OH}$ and $\text{SO}_4^{\bullet-}$ were quenched. Additionally, employing the p-CBA probe method yielded more robust evidence, corroborating the tangible role of ROS (Fig. S11). These results collectively confirmed that h^+ , $\text{O}_2^{\bullet-}$, and $^1\text{O}_2$ played major roles in the degradation of BPA. Interestingly, the results of CP and OCP tests in the PC-PMS system were consistent with the heterogeneous catalytic system (Fig. 4g-h), showing that BPA was oxidized and degraded through direct ETP in the PC-PMS system. Therefore, it can be concluded that h^+ , $\text{O}_2^{\bullet-}$, $^1\text{O}_2$, as well as ETP are responsible for BPA degradation in the PC-PMS system, which is different from the heterogeneous catalytic system.

Electron paramagnetic resonance (EPR) was employed to confirm the generation of $\text{O}_2^{\bullet-}$ and $^1\text{O}_2$ under different conditions [35]. 5,5-dimethyl-1-pyrroline-N-oxide (DMPO) was used to combine with $\text{O}_2^{\bullet-}$ to generate DMPO- $\text{O}_2^{\bullet-}$, while TEMP was used to capture $^1\text{O}_2$ to form TEMP- $^1\text{O}_2$. As shown in Fig. S12a-b, quadruple peaks at a relative intensity ratio of 1:1:1:1 and triplet signals at a relative intensity ratio of 1:1:1 were observed, attributing to characteristic peaks of TEMP- $^1\text{O}_2$ and DMPO- $\text{O}_2^{\bullet-}$, respectively. Compared to Vis/CN/PMS, Vis/CN, Vis/PMS, and Vis/CN-TDC-40 systems, the TEMP- $^1\text{O}_2$ and DMPO- $\text{O}_2^{\bullet-}$ signals in Vis/CN-TDC-40/PMS were significantly enhanced. This corresponds to the quenching results, proving that $\text{O}_2^{\bullet-}$ and $^1\text{O}_2$ play dominant roles in BPA removal.

The pathways for the formation of $\text{O}_2^{\bullet-}$ and $^1\text{O}_2$ were investigated

using EPR tests with DMPO and TEMP as radical spin-trapping agents under different conditions [36]. When operating under anoxic conditions, an obvious decrease emerged in the signal intensity of DMPO- $\text{O}_2^{\bullet-}$, indicating that dissolved oxygen (DO) was a source of $\text{O}_2^{\bullet-}$ (Fig. S13). Similarly, upon the elimination of DO, a comparable inhibitory effect was noted in the signal intensity of TEMP- $^1\text{O}_2$, suggesting that $^1\text{O}_2$ originates from DO derived $\text{O}_2^{\bullet-}$ (Fig. 4i). Moreover, the addition of EDTA resulted in a noticeable decline in the signal intensity of TEMP- $^1\text{O}_2$, indicating the pivotal role of h^+ in the formation of $^1\text{O}_2$. Consequently, it can be concluded that the generation of $^1\text{O}_2$ stems from the oxidation processes involving both $\text{O}_2^{\bullet-}$ and PMS by holes. Additionally, it is worth noting that PMS also underwent a self-decomposition process, contributing to the generation of $^1\text{O}_2$.

3.4. Degradation products and ecotoxicity evaluation

The intermediates in BPA degradation process were identified by HPLC-MS. Fig. S14 presented the detection of nine intermediates, and their corresponding spectra were displayed in Fig. S15. Electrostatic potential distribution and Fukui index (nucleophilic index f^+ and electrophilic index f^-) were adopted to predict the attacked sites on BPA molecular. As shown in Fig. S16a-b, the hydroxyl carbon and two benzene rings exhibited negative and positive electrostatic potential, respectively. Besides, the HOMO and LUMO of BPA were located on the symmetrical aromatic ring (Fig. S16c-d), suggesting susceptibility to electrophilic or nucleophilic attacks. Notably, Fig. S16e showed that O16, O17, C4, and C11 in BPA possessed the highest electrophilic attack (f^-) values, making them vulnerable to electrophilic attacks (h^+ , $^1\text{O}_2$). On the other hand, C10, C5, C3, and C12 exhibited high nucleophilic attack (f^+) values, indicating their potential for direct attacks by $\text{O}_2^{\bullet-}$. The highest free radical attack (f^0) values were calculated for C5 and C10 in BPA molecules, indicating their susceptibility to attacks by free radical ($\bullet\text{OH}$).

Combined with the theoretical calculations and intermediate products detected by HPLC-MS, three potential transformation mechanism routes of BPA are illustrated in Fig. S16f: (i) demethylation, (ii) β -scission, and (iii) hydroxylation. In Pathway 1, electrophilic attacks by h^+ and $^1\text{O}_2$ on O16, O17, C4, and C11 in BPA lead to the formation of compound A ($m/z = 199$) and compound B ($m/z = 199$) through demethylation and dehydroxylation processes. In Pathway 2, the two benzene rings (C10, C5, C3, and C12) in BPA are susceptible to nucleophilic attacks by $\text{O}_2^{\bullet-}$, resulting in β -cleavage and oxidation reactions to produce compound C ($m/z = 138$). In Pathway 3, C5 and C10 on BPA are attacked by $\bullet\text{OH}$ and $\text{SO}_4^{\bullet-}$ free radicals in the Vis/CN-TDC-40/PMS system during the hydroxylation process to form compound E ($m/z = 243$), which is subsequently cleaved to compound D ($m/z = 149$) or undergoes nucleophilic attack ($\text{O}_2^{\bullet-}$) on the aromatic ring to form compound F ($m/z = 275$) [37]. In subsequent steps, the above intermediates are further oxidized to small molecules ring-opening products G ($m/z = 127$), H ($m/z = 98$), and I ($m/z = 90$). The ecotoxicity of these intermediates was also estimated by the ECOSAR program [38], and the results are presented in Table S4. Evidently, the toxicity of the intermediates to aquatic organisms is lower than that of BPA.

3.5. BIEF study

To gain a deeper understanding of the enhanced activation mechanism of PMS on CN-TDC-40, we conducted DFT calculations to investigate the electronic structure and electron-transfer behavior of CN and TDC-incorporated heptazine motif (CN-TDC-m). The energy band structures were analyzed and depicted in Fig. S17. The work functions (ϕ) of CN and CN-TDC-m were calculated to determine the BIEF in CN-TDC-40 samples, of which the values were estimated to be 6.07 and 5.93 eV, respectively (Fig. 5a-b and Table S5). As such, electrons of CN-TDC-m with a low work function preferred to be transferred to CN units with a high work function, aligning their Fermi energy levels to the

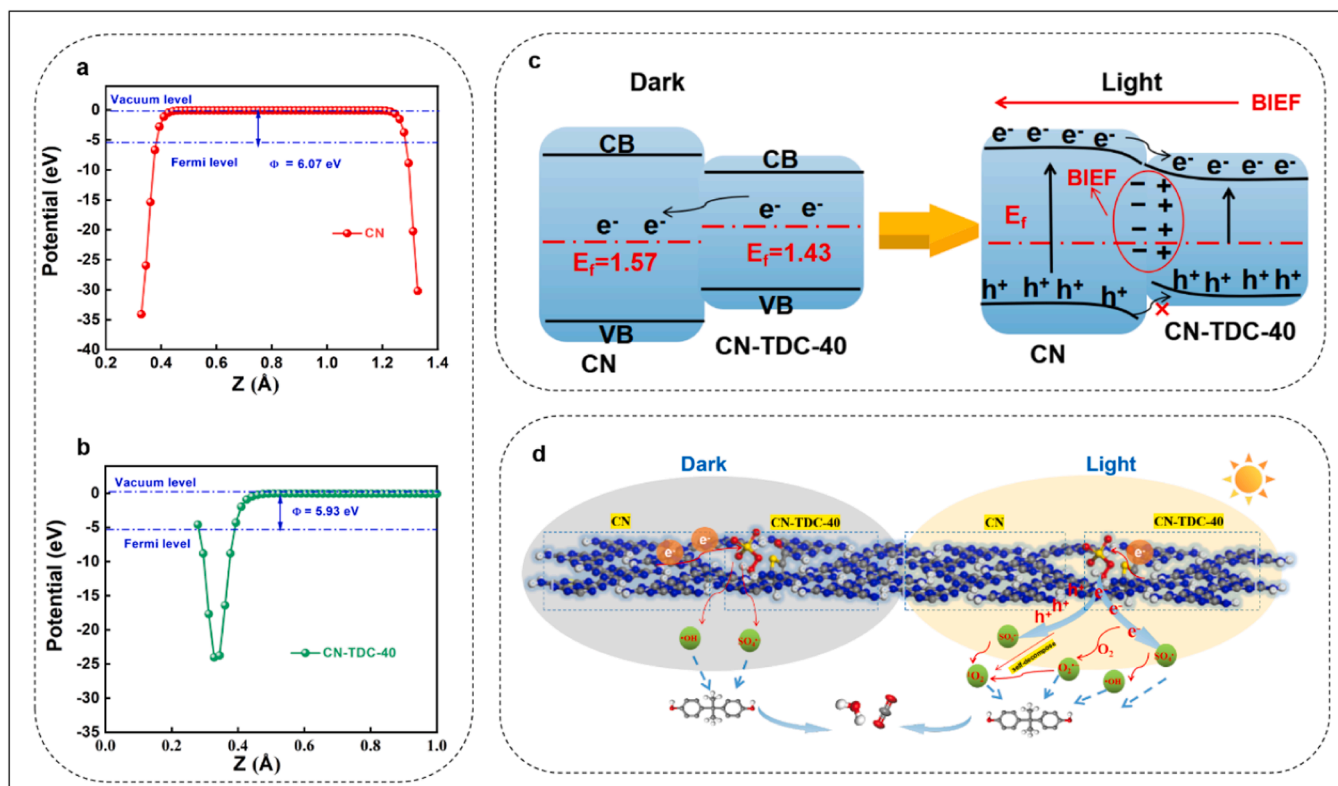


Fig. 5. The calculated work function of (a) CN and (b) CN-TDC-40; (c) Band structures of CN-TDC-40 before and after the alignment of the Fermi levels; (d) PMS activation mechanism on CN-TDC-40 in PC-PMS system.

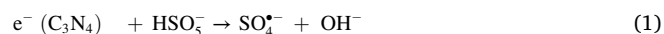
equilibrium. In this case, the Fermi levels (E_F) were calculated to be 1.57 eV for CN and 1.43 eV for the motif of CN-TDC (CN-TDC-m) with respect to the normal hydrogen electrode (NHE) (Table S5). As a result, CN accumulates a negative charge, while CN-TDC-m becomes positively charged, leading to the formation of a BIEF directed from CN-TDC-m to CN at the contact of CN-TDC-40 (as illustrated in Fig. 5c) even in the absence of light. This BIEF adjusts the surface charge distribution of the catalyst, causing electron rearrangement at the interfacial region.

In the dark, as illustrated in Fig. 5d, the electron-rich CN part acts as the electron donor, while PMS serves as the electron acceptor, resulting in the generation of $\text{SO}_4^{\bullet-}$ and $\bullet\text{OH}$. In the PC-PMS system, photo-excited electrons in the CN region flow smoothly into the CB of CN-TDC-m, becoming concentrated on the CB of CN-TDC-m for PMS activation. This leads to the formation of electron-rich centers in CN-TDC-m and electron-deficient centers in the nearby CN. The readjustment of Fermi levels causes band bending of both compositions, resulting in upward shifts of the CB and VB of CN and downward shifts of the CB and VB of CN-TDC-m. This expands the distance between the CBs of the two components and promotes higher electron transfer. Although holes tend to migrate from the VB of CN to CN-TDC-m, they are restricted by the strong steric hindrance of the BIEF and remain in both components [39]. This leads to both CN and CN-TDC-m participating in the activation of PMS, as confirmed by the XPS survey of CN-TDC-40 before and after activation, as shown in Fig. S18 and Table S6. As a result, the dual charge modulation induced by BIEF enables the maximum utilization of photogenerated electrons and holes for pollutant degradation.

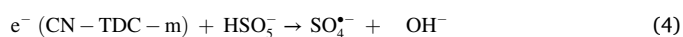
To delve into the BIEF present in CN and CN-TDC-40 samples, we employed in situ light irradiation Kelvin probe force microscope (KPFM) technique to gauge their surface potentials both before and after light illumination. The visual representation in Fig. S19 elucidates this phenomenon. It is intriguing to note that in the absence of light, the surface potential (ΔE) exhibited a higher value in CN-TDC-40 (35.3 mV) compared to CN (32.1 mV), suggesting an enlarged BIEF upon the introduction of TDC rings into the carbon nitride matrix. Upon the

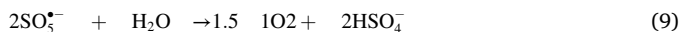
application of light irradiation, the surface potential of CN and CN-TDC-40 experienced increases of 3.3 and 8.6 mV, respectively. This outcome from KPFM seamlessly aligns with the findings derived from DFT analyses, effectively corroborating the boosted charge separation and transportation observed in CN-TDC-40, attributable to its larger BIEF.

Based on the above analysis, a proposed mechanism for PMS activation in the heterogeneous process and the photo-assisted PMS activation on the CN-TDC-40 catalyst can be outlined. In the dark, PMS acted as an electron acceptor and was reduced to produce $\text{SO}_4^{\bullet-}$ and $\bullet\text{OH}$. (Eqs. (1 and 2)).



In the PC-PMS activation system, the generated e^- in CN-TDC-m can activate PMS to produce $\text{SO}_4^{\bullet-}$ and $\bullet\text{OH}$ (Eqs. (3–5)), but the $\text{SO}_4^{\bullet-}$ and $\bullet\text{OH}$ played a minor role in BPA oxidation. Additionally, it is noted that the CB site (−0.83 eV) of the CN-TDC-40 catalyst is higher than the redox potential (−0.33 eV) of $\text{O}_2/\text{O}_2^{\bullet-}$, indicating the thermodynamic feasibility of $\text{O}_2^{\bullet-}$ generation from photogenerated electrons (Eq. (6)). Simultaneously, holes react with $\text{O}_2^{\bullet-}$ to generate $^1\text{O}_2$ (Eq. (7)). Holes also combine with hydrogen sulfate (HSO_5^-) to produce persulfate ($\text{SO}_5^{\bullet-}$) radicals, which rapidly self-react to generate $^1\text{O}_2$ due to the high reaction rate and low activation energy (Eqs. (8 and 9)) [6]. PMS also undergoes self-decompose to form $^1\text{O}_2$ in an aqueous solution as previously reported (Eq. (10)) [36]. Finally, h^+ , $\text{O}_2^{\bullet-}$, $^1\text{O}_2$, and ETP contribute to the degradation of BPA.





3.6. Modulation mechanism of BIEF

The activation of PMS is directly influenced by the adsorption energies (E_{ads}) of PMS molecules [40]. The adsorption configurations and bond length information of PMS on CN and CN-TDC-40 in the dark were investigated (Fig. 6a-b and Table S7). The bond length of the O-O bond of PMS molecules was prolonged from 1.438 Å to 1.479 Å and 1.496 Å on CN and CN-TDC-40, respectively, demonstrating that CN-TDC-40 is more favorable for cleaving the O-O bond of PMS molecules to form active species. The corresponding adsorption energy (E_{ads}) of PMS on CN (−2.64 eV) was higher than that of CN-TDC-40 (−2.93 eV) (Fig. S20), suggesting that CN-TDC-40 has a higher affinity for PMS adsorption, reducing the activation energy barrier of PMS. Meanwhile, the adsorption structure model reveals that PMS is primarily adsorbed on the thiophene ring of CN-TDC-40 rather than on CN. However, CN serves as the reaction site that activates PMS in the dark. This explains the relatively poor degradation efficiency of BPA in the heterogeneous catalytic process. Conversely, in the photo-assisted PMS activation system, CN-TDC-m functions as both the reaction site and the adsorption site, thereby exhibiting excellent performance.

The analysis of electrostatic potential distribution can further predict the likely sites of chemical reactions. Generally, atoms with positive (negative) electrostatic potential are prone to undergo electrophilic (nucleophilic) chemical reactions [41]. As observed in Fig. 6c-d, the electrostatic potential of CN is negative, indicating its susceptibility to nucleophilic attack by PMS, leading to the generation of ROS for the oxidation of organic compounds. This observation is in line with the aforementioned experimental results, confirming the nucleophilic reactivity of CN with PMS.

The impact of BIEF on the enhanced PC-PMS process was then investigated. UV-Vis diffuse reflectance spectroscopy (DRS) was performed to examine the optical properties of CN and CN-TDC-X (Fig. 6e). The absorption edge of CN was observed at around 460 nm. However, the incorporation of TDC rings in CN-TDC-X led to extended absorption into the near-infrared region, accompanied by the color of the prepared sample ranging from light yellow to dark brown (Fig. S21), indicating its potential for harnessing full-spectrum sunlight. The bandgap energies were estimated to be 2.82, 2.76, 2.63, and 2.53 eV vs. NHE for CN, CN-TDC-20, CN-TDC-40, and CN-TDC-60, respectively (Fig. S22a). The corresponding valence band positions (VB) were measured as 1.95, 2.08, 1.80, and 1.85 V vs. NHE, respectively (Fig. S22b). The band structures were depicted in Fig. S22c. Notably, CN-TDC-40 exhibited a narrower bandgap compared to pure CN, indicating its suitability for efficient electronic transitions between energy levels.

Photoluminescence (PL) technique was employed to investigate the recombination behavior of photoinduced carriers [42]. As depicted in Fig. 6f, the fluorescence intensity of CN-TDC-X was significantly decreased when compared with that of CN, suggesting a substantial reduction in electron-hole recombination. Electron paramagnetic resonance (EPR) was performed to determine the concentration of unpaired electrons in the synthesized samples (Fig. 6g). All samples displayed a characteristic signal with a g value of 2.001, attributed to the unpaired electron in the CN framework. The concentration of hot electrons on the catalyst was estimated by calculating the difference in the twice-integrated areas of the EPR signal [43]. The integrated area difference for CN-TDC-40 before and after light irradiation was

significantly higher than that of CN, indicating the highest number of hot electrons after the fabrication of BIEF.

Time-resolved photoluminescence spectra (TR-PL) were used to monitor the lifetime of charge carriers (Fig. 6h). The τ values of CN and CN-TDC-40 were measured to be 6.77 and 5.49 ns, respectively (Table S8). The shorter lifetime of CN-TDC-40 signifies that the incorporation of TDC into carbon nitride enhances electron migration and improves carrier separation efficiency. Electrochemical impedance spectroscopy (EIS) was conducted to evaluate the interfacial charge transfer in CN and CN-TDC-40. As shown in Fig. 6i, the arc radius of CN-TDC-40 was smaller than that of CN, meaning a lower charge transport resistance in CN-TDC-40. Furthermore, the photocurrent of CN-TDC-40 exceeded that of CN (Fig. 6j), providing additional evidence of enhanced carrier separation and transportation rates. The aforementioned improvements in photoelectric performance are primarily attributed to the efficient charge transfer channel facilitated by the dual charge modulation of the established BIEF.

The effective charge separation in CN-TDC-40 was further illustrated by the calculated HOMO and LUMO. The optimized cell models for CN and CN-TDC-40 are depicted in Fig. S23a and d. In contrast to the evenly distributed electron holes in CN (Fig. S23b-c), the incorporation of TDC resulted in a pronounced separation of holes in HOMO and electrons in LUMO. Specifically, the electrons were localized around the tri-s-triazine motifs in LUMO, while the holes were localized around the CN-TDC-m in HOMO (Fig. S23e-f). This asymmetry contributed to the generation of potential differences and alterations in the electronic structure, which facilitated persulfate activation under visible light irradiation.

As mentioned above, BIEF achieves efficient activation of PMS through a dual charge modulation mechanism in the BPA degradation process. In heterogeneous catalysis without light, the insertion of thiophene rings leads to charge imbalance, resulting in the formation of BIEF from CN-TDC-40 to CN. PMS acts as an electron acceptor, acquiring electrons from the electron-rich CN, ultimately leading to PMS reduction around the electron-rich CN. When exposed to visible light, the optical absorption capability and the charge dynamics are significantly improved endowed by the BIEF. CN-TDC-m becomes an electron-rich center, while CN acted as an electron-deficient center. On one hand, PMS undergoes a reduction reaction on the electron-rich CN-TDC-m, which serves as a reaction site to reduce the activation energy barrier of PMS. On the other hand, PMS was oxidized by holes to generate $^1\text{O}_2$. As a result, h^{+} , $\text{O}_2^{\bullet -}$, $^1\text{O}_2$, and ETP are dominant in the PC-PMS system for a nearly 100% degradation rate within 40 min.

4. Conclusions

In summary, we have incorporated thiophene rings into polymeric carbon nitride, which was used for PC-PMS activation toward water purification and served as a platform to investigate the modulation mechanism of BIEF. The Vis/CN-TDC-40/PMS system demonstrates outstanding performance in the removal of BPA, achieving complete removal within 40 min. Comprehensive characterization techniques and DFT calculations have elucidated the dual charge modulation and dual PMS activation mechanism of BIEF in the PC-PMS system. In the dark, a BIEF in CN-TDC-40 leads to the reduction of PMS at the electron-rich region of CN. In PC-PMS system, electrons accumulate in the conduction band of CN-TDC-m, while holes are localized in the valence bands of CN and CN-TDC-m. PMS undergoes redox reactions, resulting in the generation of h^{+} , $^1\text{O}_2$, $\bullet\text{O}_2^{-}$, and ETP pathway. Consequently, the heterogeneous catalysis and PC-PMS coupling system are simultaneously modulated by BIEF. The formed BIEF not only enhances PMS adsorption and reduces the activation energy barrier but also optimizes the electronic structure, expands the absorption range of visible light, and improves carrier separation. The findings of this work provide crucial insights into the modulation mechanism of the PC-PMS system driven by BIEF, offering valuable guidance for catalyst development and

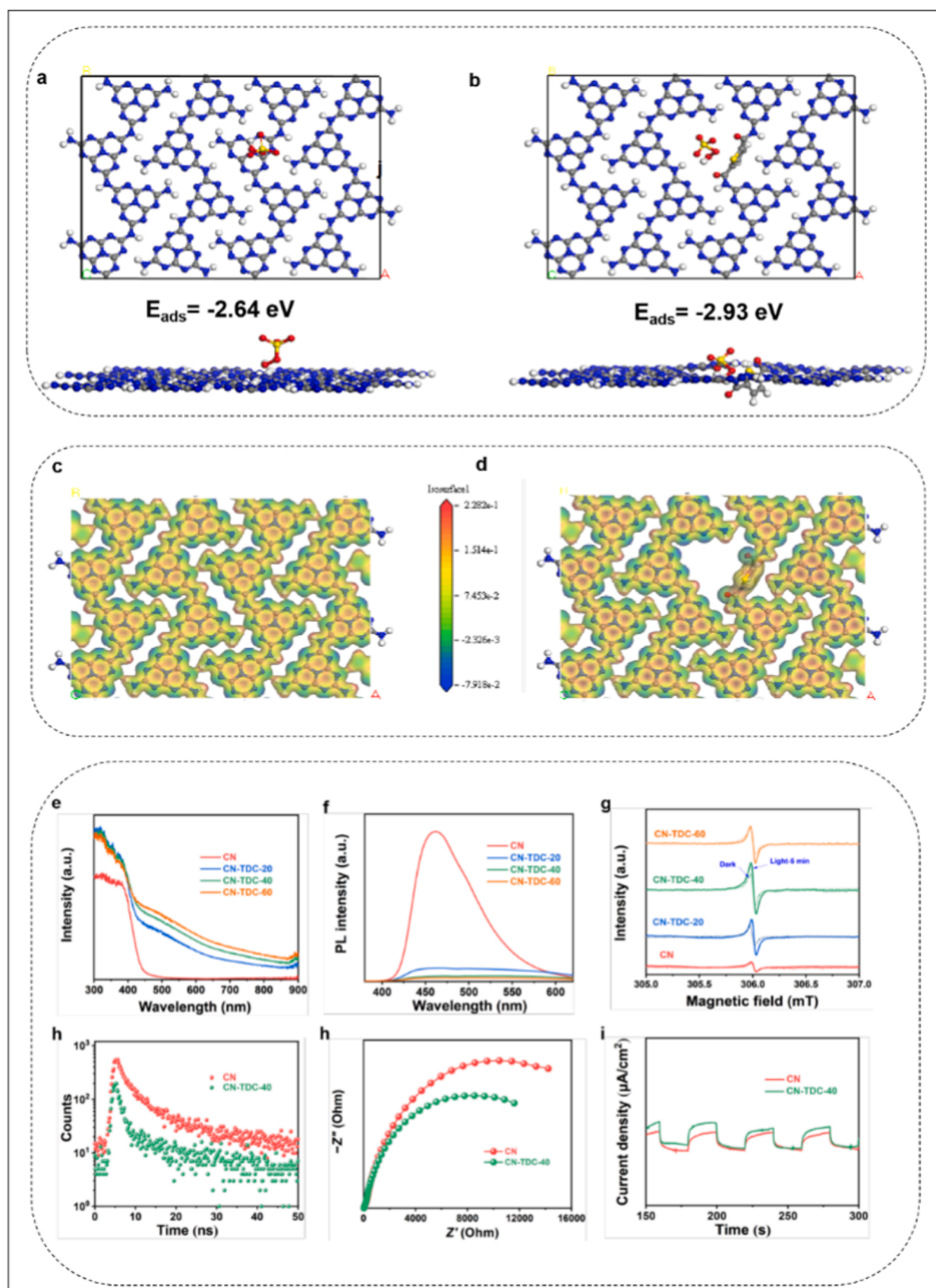


Fig. 6. Top and side views of the optimal adsorption configurations of PMS adsorbed on (a) CN and (b) CN-TDC-40; Electrostatic potential distribution of (c) CN and (d) CN-TDC-40 (red and blue represents positive and negative potential, respectively); (e) UV-vis DRS measurements, (f) PL results, and (g) solid EPR spectra of CN and CN-TDC-X; (h) TR-PL spectra, (i) EIS plots, and (j) I-T curves of CN and CN-TDC-40.

sustainable wastewater purification.

CRediT authorship contribution statement

Fengting He: Methodology, Data curation, Writing – original draft, Visualization. **Yangming Lu:** DFT computational resources, Investigation. **Guofei Jiang:** Software. **Yang Zhang:** Data curation. **Pei Dong:** Resources. **Xiaoming Liu:** Investigation. **Yongqiang wang:** Supervision. **Chaocheng Zhao:** Project administration, Funding acquisition. **Shuaijun Wang:** Writing – review & editing, Supervision. **Xiaoguang Duan:** Validation, Supervision. **Jinqiang Zhang:** Conceptualization, Writing – review & editing, Supervision. **Shaobin Wang:** Data curation, Supervision.

Declaration of Competing Interest

The authors declare that they have no known competing financial interests or personal relationships that could have appeared to influence the work reported in this paper.

Data availability

Data will be made available on request.

Acknowledgment

This work was supported by the National Science and Technology Major Project (Grant No. 2016ZX05040003).

Appendix A. Supporting information

Supplementary data associated with this article can be found in the online version at [doi:10.1016/j.apcatb.2023.123307](https://doi.org/10.1016/j.apcatb.2023.123307).

References

- C. He, Z. Liu, J. Wu, X. Pan, Z. Fang, J. Li, B.A. Bryan, Future global urban water scarcity and potential solutions, *Nat. Commun.* 12 (2021) 4667, <https://doi.org/10.1038/s41467-021-25026-3>.
- F. Dolan, J. Lamontagne, R. Link, M. Hejazi, P. Reed, J. Edmonds, Evaluating the economic impact of water scarcity in a changing world, *Nat. Commun.* 12 (2021) 1915, <https://doi.org/10.1038/s41467-021-22194-0>.
- Y. Zhou, J. Jiang, Y. Gao, S.Y. Pang, J. Ma, J. Duan, Q. Guo, J. Li, Y. Yang, Oxidation of steroid estrogens by peroxymonosulfate (PMS) and effect of bromide and chloride ions: Kinetics, products, and modeling, *Water Res.* 138 (2018) 56–66, <https://doi.org/10.1016/j.watres.2018.03.045>.
- H. Li, Z. Zhao, J. Qian, B. Pan, Are free radicals the primary reactive species in co (ii)-mediated activation of peroxymonosulfate? New evidence for the role of the co (ii)-peroxymonosulfate complex, *Environ. Sci. Technol.* 55 (2021) 6397–6406, <https://doi.org/10.1021/acs.est.1c02015>.
- S. Zhu, X. Li, J. Kang, X. Duan, S. Wang, Persulfate activation on crystallographic manganese oxides: mechanism of singlet oxygen evolution for nonradical selective degradation of aqueous contaminants, *Environ. Sci. Technol.* 53 (2019) 307–315, <https://doi.org/10.1021/acs.est.8b04669>.
- L.S. Zhang, X.H. Jiang, Z.A. Zhong, L. Tian, Q. Sun, Y.T. Cui, X. Lu, J.P. Zou, S. L. Luo, Carbon nitride supported high-loading Fe single-atom catalyst for activation of peroxymonosulfate to generate $^1\text{O}_2$ with 100% selectivity, *Angew. Chem. Int. Ed.* 60 (2021) 21751–21755, <https://doi.org/10.1002/anie.202109488>.
- H. Wang, W. Guo, B. Liu, Q. Si, H. Luo, Q. Zhao, N. Ren, Sludge-derived biochar as efficient persulfate activators: sulfuration-induced electronic structure modulation and disparate nonradical mechanisms, *Appl. Catal., B-Environ.* 279 (2020), 119361, <https://doi.org/10.1016/j.apcatb.2020.119361>.
- C. Fu, M. Zhao, X. Chen, G. Sun, C. Wang, Q. Song, Unraveling the dual defect effects in C_3N_4 for piezo-photocatalytic degradation and H_2O_2 generation, *Appl. Catal., B-Environ.* 332 (2023), 122752, <https://doi.org/10.1016/j.apcatb.2023.122752>.
- Y. Deng, J. Liu, Y. Huang, M. Ma, K. Liu, X. Dou, Z. Wang, S. Qu, Z. Wang, Engineering the photocatalytic behaviors of $\text{g-C}_3\text{N}_4$ based metal-free materials for degradation of a representative antibiotic, *Adv. Funct. Mater.* 30 (2020), 2002353, <https://doi.org/10.1002/adfm.202002353>.
- B. Liu, W. Guo, W. Jia, H. Wang, Q. Si, Q. Zhao, H. Luo, J. Jiang, N. Ren, Novel nonradical oxidation of sulfonamide antibiotics with Co(ii)-doped $\text{g-C}_3\text{N}_4$ -activated peracetic acid: role of high-valent cobalt-oxo species, *Environ. Sci. Technol.* 55 (2021) 12640–12651, <https://doi.org/10.1021/acs.est.1c04091>.
- J. Zhang, X. Zhao, Y. Wang, Y. Gong, D. Cao, M. Qiao, Peroxymonosulfate-enhanced visible light photocatalytic degradation of bisphenol A by perylene imide-modified $\text{g-C}_3\text{N}_4$, *Appl. Catal., B-Environ.* 237 (2018) 976–985, <https://doi.org/10.1016/j.apcatb.2018.06.049>.
- Y. Guo, W. Shi, Y. Zhu, Internal electric field engineering for steering photogenerated charge separation and enhancing photoactivity, *EcoMat* 1 (2019), e12007, <https://doi.org/10.1002/eom2.12007>.
- D. Chen, R. Lu, R. Yu, Y. Dai, H. Zhao, D. Wu, P. Wang, J. Zhu, Z. Pu, L. Chen, J. Yu, S. Mu, Work-function-induced interfacial built-in electric fields in Os-OsSe_2 heterostructures for active acidic and alkaline hydrogen evolution, *Angew. Chem. Int. Ed.* 61 (2022), e202208642, <https://doi.org/10.1002/anie.202208642>.
- I. Grić, G. Li Puma, Six-flux absorption-scattering models for photocatalysis under wide-spectrum irradiation sources in annular and flat reactors using catalysts with different optical properties, *Appl. Catal., B-Environ.* 211 (2017) 222–234, <https://doi.org/10.1016/j.apcatb.2017.04.014>.
- G. Li Puma, A. Brucato, Dimensionless analysis of slurry photocatalytic reactors using two-flux and six-flux radiation absorption-scattering models, *Catal. Today* 122 (2007) 78–90, <https://doi.org/10.1016/j.cattod.2007.01.027>.
- R. Acosta-Herazo, M.Á. Mueses, G.L. Puma, F. Machuca-Martínez, Impact of photocatalyst optical properties on the efficiency of solar photocatalytic reactors rationalized by the concepts of initial rate of photon absorption (IRPA) dimensionless boundary layer of photon absorption and apparent optical thickness, *Chem. Eng. J.* 356 (2019) 839–849, <https://doi.org/10.1016/j.cej.2018.09.085>.
- R. Peralta Muniz Moreira, G. Li Puma, Multiphysics computational fluid-dynamics (CFD) modeling of annular photocatalytic reactors by the discrete ordinates method (DOM) and the six-flux model (SFM) and evaluation of the contaminant intrinsic kinetics constants, *Catal. Today* 361 (2021) 77–84, <https://doi.org/10.1016/j.cattod.2020.01.012>.
- P. Shao, Y. Jing, X. Duan, H. Lin, L. Yang, W. Ren, F. Deng, B. Li, X. Luo, S. Wang, Revisiting the graphitized nanodiamond-mediated activation of peroxymonosulfate: Singlet oxygenation versus electron transfer, *Environ. Sci. Technol.* 55 (2021) 16078–16087, <https://doi.org/10.1021/acs.est.1c02042>.
- Y. Lu, J. Liang, Y. Hu, Y. Liu, K. Chen, S. Deng, D. Wang, Accurate control multiple active sites of carbonaceous anode for high performance sodium storage: Insights into capacitive contribution mechanism, *Adv. Energy Mater.* 10 (2020), 1903312, <https://doi.org/10.1002/aenm.201903312>.
- S. Wang, F. He, X. Zhao, J. Zhang, Z. Ao, H. Wu, Y. Yin, L. Shi, X. Xu, C. Zhao, S. Wang, H. Sun, Phosphorous doped carbon nitride nanobelts for photodegradation of emerging contaminants and hydrogen evolution, *Appl. Catal., B-Environ.* 257 (2019), 117931, <https://doi.org/10.1016/j.apcatb.2019.117931>.
- N. Sun, Y. Liang, X. Ma, F. Chen, Reduced oxygenated $\text{g-C}_3\text{N}_4$ with abundant nitrogen vacancies for visible-light photocatalytic applications, *Chem. Eur. J.* 23 (2017) 15466–15473, <https://doi.org/10.1002/chem.201703168>.
- Y. Guo, Z. Zeng, Y. Zhu, Z. Huang, Y. Cui, J. Yang, Catalytic oxidation of aqueous organic contaminants by persulfate activated with sulfur-doped hierarchically porous carbon derived from thiophene, *Appl. Catal., B-Environ.* 220 (2018) 635–644, <https://doi.org/10.1016/j.apcatb.2017.08.073>.
- O. Unsalan, Y. Erdogdu, M.T. Gulluoglu, FT-Raman and FT-IR spectral and quantum chemical studies on some flavonoid derivatives: baicalein and Naringenin, *J. Raman Spectrosc.* 40 (2009) 562–570, <https://doi.org/10.1002/jrs.2166>.
- D. Vidyasagar, S.G. Ghugal, S.S. Umare, M. Banavoth, Extended π -conjugative n-p type homostructural graphitic carbon nitride for photodegradation and charge-storage applications, *Sci. Rep.* 9 (2019) 7186, <https://doi.org/10.1038/s41598-019-43312-5>.
- Y. Guo, J. Li, Y. Yuan, L. Li, M. Zhang, C. Zhou, Z. Lin, A rapid microwave-assisted thermolysis route to highly crystalline carbon nitrides for efficient hydrogen generation, *Angew. Chem. Int. Ed.* 55 (2016) 14693–14697, <https://doi.org/10.1002/anie.201608453>.
- J. Zhang, G. Zhang, X. Chen, S. Lin, L. Mohlmann, G. Dolega, G. Lipner, M. Antonietti, S. Blechert, X. Wang, Co-monomer control of carbon nitride semiconductors to optimize hydrogen evolution with visible light, *Angew. Chem. Int. Ed.* 51 (2012) 3183–3187, <https://doi.org/10.1002/anie.201106656>.
- S. Zhao, X. Zhao, H. Zhang, J. Li, Y. Zhu, Covalent combination of polyoxometalate and graphitic carbon nitride for light-driven hydrogen peroxide production, *Nano Energy* 35 (2017) 405–414, <https://doi.org/10.1016/j.nanoen.2017.04.017>.
- F. Ge, S. Huang, J. Yan, L. Jing, F. Chen, M. Xie, Y. Xu, H. Xu, H. Li, Sulfur promoted $n-\pi^*$ electron transitions in thiophene-doped $\text{g-C}_3\text{N}_4$ for enhanced photocatalytic activity, *Chin. J. Catal.* 42 (2021) 450–459, [https://doi.org/10.1016/s1872-0667\(20\)63674-9](https://doi.org/10.1016/s1872-0667(20)63674-9).
- C. Zhang, Z. Ouyang, Y. Yang, X. Long, L. Qin, W. Wang, Y. Zhou, D. Qin, F. Qin, C. Lai, Molecular engineering of donor-acceptor structured $\text{g-C}_3\text{N}_4$ for superior photocatalytic oxytetracycline degradation, *Chem. Eng. J.* 448 (2022), 137370, <https://doi.org/10.1016/j.cej.2022.137370>.
- F. Chen, X.L. Wu, C. Shi, H. Lin, J. Chen, Y. Shi, S. Wang, X. Duan, Molecular engineering toward pyrrolic N-Rich M- N_4 (M = Cr, Mn, Fe, Co, Cu) Single-Atom Sites for Enhanced Heterogeneous Fenton-Like Reaction, *Adv. Funct. Mater.* 31 (2021), 2007877, <https://doi.org/10.1002/adfm.202007877>.
- L. Wang, B. Li, D.D. Dionysiou, B. Chen, J. Yang, J. Li, Overlooked formation of H_2O_2 during the hydroxyl radical-scavenging process when using alcohols as scavengers, *Environ. Sci. Technol.* 56 (2022) 3386–3396, <https://doi.org/10.1021/acs.est.1c03796>.
- Y. Gao, Z. Chen, Y. Zhu, T. Li, C. Hu, New insights into the generation of singlet oxygen in the metal-free peroxymonosulfate activation process: important role of electron-deficient carbon atoms, *Environ. Sci. Technol.* 54 (2020) 1232–1241, <https://doi.org/10.1021/acs.est.9b05856>.

- [33] E.T. Yun, J.H. Lee, J. Kim, H.D. Park, J. Lee, Identifying the nonradical mechanism in the peroxymonosulfate activation process: singlet oxygenation versus mediated electron transfer, *Environ. Sci. Technol.* 52 (2018) 7032–7042, <https://doi.org/10.1021/acs.est.8b00959>.
- [34] Y. Zhou, J. Jiang, Y. Gao, J. Ma, S.Y. Pang, J. Li, X.T. Lu, L.P. Yuan, Activation of peroxymonosulfate by benzoquinone: a novel nonradical oxidation process, *Environ. Sci. Technol.* 49 (2015) 12941–12950, <https://doi.org/10.1021/acs.est.5b03595>.
- [35] Y. Guo, J. Long, J. Huang, G. Yu, Y. Wang, Can the commonly used quenching method really evaluate the role of reactive oxygen species in pollutant abatement during catalytic ozonation? *Water Res.* 215 (2022), 118275 <https://doi.org/10.1016/j.watres.2022.118275>.
- [36] J. Wang, S. Wang, Activation of persulfate (PS) and peroxymonosulfate (PMS) and application for the degradation of emerging contaminants, *Chem. Eng. J.* 334 (2018) 1502–1517, <https://doi.org/10.1016/j.cej.2017.11.059>.
- [37] W.-D. Oh, L.-W. Lok, A. Veksha, A. Giannis, T.-T. Lim, Enhanced photocatalytic degradation of bisphenol A with Ag-decorated S-doped g-C₃N₄ under solar irradiation: Performance and mechanistic studies, *Chem. Eng. J.* 333 (2018) 739–749, <https://doi.org/10.1016/j.cej.2017.09.182>.
- [38] Y. Li, M. Xie, S. Zhang, L. Zhao, L. Kong, J. Zhan, R.-S. Zhao, Porous 3D superstructure of nitrogen doped carbon decorated with ultrafine cobalt nanodots as peroxymonosulfate activator for the degradation of sulfonamides, *Chem. Eng. J.* 428 (2022), 131329, <https://doi.org/10.1016/j.cej.2021.131329>.
- [39] X. Ma, H. Cheng, Synergy of nitrogen vacancies and intercalation of carbon species for enhancing sunlight photocatalytic hydrogen production of carbon nitride, *Appl. Catal., B-Environ.* 314 (2022), 121497, <https://doi.org/10.1016/j.apcatb.2022.121497>.
- [40] F. Chen, L.L. Liu, J.J. Chen, W.W. Li, Y.P. Chen, Y.J. Zhang, J.H. Wu, S.C. Mei, Q. Yang, H.Q. Yu, Efficient decontamination of organic pollutants under high salinity conditions by a nonradical peroxymonosulfate activation system, *Water Res.* 191 (2021), 116799, <https://doi.org/10.1016/j.watres.2020.116799>.
- [41] B. Zhu, S. Chen, C. Li, G. Jiang, F. Liu, R. Zhao, C. Liu, Non-metallic hollow porous sphere loaded CN/catalytic ozonation synergistic photocatalytic system: Enhanced treatment of emerging pollutants by three-stage cyclic reaction mechanism, *Appl. Catal., B-Environ.* 318 (2022), 121881, <https://doi.org/10.1016/j.apcatb.2022.121881>.
- [42] Q. Ji, X. Cheng, X. Kong, D. Sun, Y. Wu, Z. Xu, Y. Liu, X. Duan, H. He, S. Li, L. Zhang, S. Yang, Visible-light activation of persulfate ions by Z-scheme perylene diimide/MIL-101(Cr) heterojunction photocatalyst towards efficient degradation of iohexol, *Chem. Eng. J.* 435 (2022), 134947, <https://doi.org/10.1016/j.cej.2022.134947>.
- [43] Y. Jin, F. Li, T. Li, X. Xing, W. Fan, L. Zhang, C. Hu, Enhanced internal electric field in S-doped BiOBr for intercalation, adsorption and degradation of ciprofloxacin by photoinitiation, *Appl. Catal., B-Environ.* 302 (2022), 120824, <https://doi.org/10.1016/j.apcatb.2021.120824>.